Electrochemical characterization and computational fluid dynamics simulation of flow-accelerated corrosion of X65 steel in a CO$_2$-saturated oilfield formation water

G.A. Zhang, Y.F. Cheng *

Department of Mechanical and Manufacturing Engineering, University of Calgary, Calgary, AB, Canada T2N 1N4

ABSTRACT

The flow-accelerated corrosion (FAC) of an X65 pipeline steel was investigated in a CO$_2$-saturated formation water by electrochemical measurements and computational fluid dynamics (CFD) simulation on micro-electrodes installed on an impingement jet system. The surface morphology of the electrodes after corrosion test was characterized by scanning electron microscopy. Results demonstrated that the role of fluid hydrodynamics in FAC of the steel depends on its effect on the carbonate corrosion scale formed on the electrode surface. An increasing flow velocity and shear stress would thinner, degrade or even remove completely the scale, increasing corrosion of the steel. An oblique impact of fluid would generally result in a high corrosion rate of the steel. The effect of impact angle on corrosion of the steel is attributed to the distribution of fluid flow field and shear stress on the electrode surface. At the normal impact, a low flow velocity and shear stress and thus a low mass transfer rate would be generated at the centric region. Consequently, a compact corrosion scale can be formed on the electrode surface to protect the steel from corrosion. The highest corrosion rate is observed on micro-electrodes that are adjacent to the center, with the highest flow velocity and shear stress. At the oblique impact angles, the fluid flow velocity and shear stress, and the corrosion rate of the micro-electrodes are higher at the side far away from the nozzle than those at the side close to nozzle. The corrosion activity of the steel electrode located at the center of the sample holder generally increases with the decreasing impact angle due to the enhancing shear effect on the corrosion scale.

© 2010 Elsevier Ltd. All rights reserved.

1. Introduction

It is acknowledged [1–5] that CO$_2$ corrosion would cause the failure of pipelines and structural components in petroleum production, resulting in significant economic loss and catastrophic accidents as well as water resource and environmental pollution. The CO$_2$ corrosion is complex, with a number of factors affecting the corrosion process of the steel [5–10]. In particular, the fluid hydrodynamics play a significant role through a complex interrelationship of near-wall hydrodynamic momentum and mass transfer as well as fluid parameters defining general flow properties with the corrosion reactions of steel [11–15]. It is generally believed that the fluid flow would accelerate the mass transfer process and degrade the protective corrosion scale formed on the steel surface.

Flow-accelerated corrosion (FAC) contributes remarkably the degradation of pipeline steel in the CO$_2$-containing environment [16–18]. The flow field developed on the steel surface under fluid flow is quite complex, with different flow velocities and shear stresses exerted on the different locations of the electrode [14,19, 20]. It is thus expected that the steel electrode experiences a non-uniform corrosion under fluid flow. For example, the previous work on FAC of aluminum alloy in an automotive coolant [20] found that the center of the aluminum alloy electrode is associated with the most stable state, while the edge of the electrode has the most active state, which is directly related to the velocity of fluid flow and the distribution of shear stress on the electrode surface. In oil and gas transportation pipelines, the corrosion rates of the carbon steel pipe at various positions are expected to be different due to the different impact angle of the fluid to the steel. For example, the elbow bend, as an important part of the practical pipe configuration, is prone to experience FAC. It is thus of great significance to determine the effect of fluid flow and its impact angle on FAC of the steel.

In this work, the FAC behavior of an X65 pipeline steel was investigated in the CO$_2$-saturated formation water by electrochemical measurements using an impingement jet system. The flow field distribution on the electrode surface was determined by

* Corresponding author. Tel.: +1 403 220 3693; fax: +1 403 282 8406.
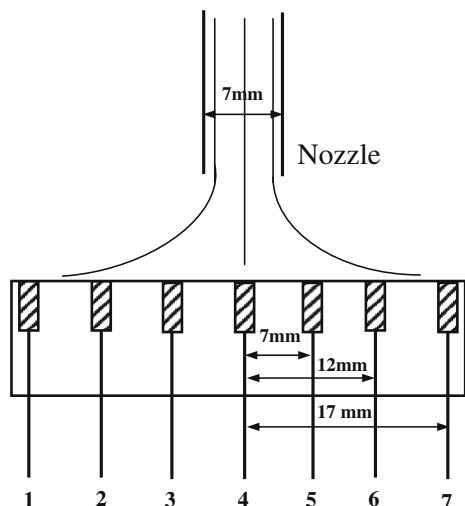 *E-mail address:* fcheng@ucalgary.ca (Y.F. Cheng).

Fig. 1. Schematic diagram of the experimental set-up of micro-electrodes under fluid impingement.

computational fluid dynamics (CFD) simulation. The surface morphology of the electrode after test was characterized by scanning electron microscopy (SEM). The role of fluid hydrodynamics in FAC of the steel was mechanistically determined.

2. Experimental

2.1. Materials and solutions

The test specimens in this work were made of a X65 steel pipe, with a chemical composition (wt.%): C 0.04%, Si 0.2%, Mn 1.5%, P 0.011%, S 0.003%, Mo 0.02% and Fe balance. The pipe steel was cut and machined into micro-electrodes with an exposure area of 1 mm × 1 mm. Seven micro-electrodes were mounted in a holder by epoxy resin, and were arranged symmetrically in radial direction, as shown in Fig. 1. All micro-electrodes were electrically connected individually by copper wires to the measurement equipment. The electrodes were ground up to 1000 grit silicon carbide paper, rinsed with deionized water and degreased in acetone.

Test solution, simulating the formation water extracted from the oil and gas field, was made up from analytical grade reagents and deionized water, with a chemical composition shown in Table 1. The solution was deaerated by purging CO_2 gas (99.95%) for 4 h prior to test. The specimen holder containing micro-electrodes was then immersed into the solution while the CO_2 gas-purging was maintained to ensure an entire saturation throughout the test. The pH value of the CO_2-saturated solution was 5.11.

All the tests were performed at room temperature (22 °C) and atmospheric pressure.

2.2. Impingement jet test

An impingement jet system developed previously [20–23] was used to conduct the FAC test. It consisted of a plexiglass chamber as a reservoir, a high pressure pump, flow velocity controller, sand concentration controller, stirrer and valves. An electrochemical cell was integrated with the test rig to enable in situ electrochemical measurements. The impact angle of the impinging fluid to working electrode, which was defined as the angle between the surface of the electrode and the fluid flow direction, can be adjusted conveniently. The total volume of the container for the bulk solution was 1 L, and the volume of the electrochemical test chamber where the electrode was installed was 150 mL.

2.3. Electrochemical measurements

Electrochemical measurements were conducted on a three-electrode cell, where the steel micro-electrode was used as working electrode, a platinum ring as counter electrode and a saturated calomel electrode (SCE) as reference electrode, using a Solartron analytical 1280C electrochemical system. All electrochemical tests were performed on the steel electrode after 12 h of exposure in the solution in order to form a layer of iron carbonate scale. The present work showed that the formation of a $FeCO_3$ scale was feasible after 12 h of exposure, which was attributed to the increased corrosion rate of the steel in the flowing solution. The increasing Fe^{2+}

Table 1
Ionic concentration of the formation water extracted from oil field.

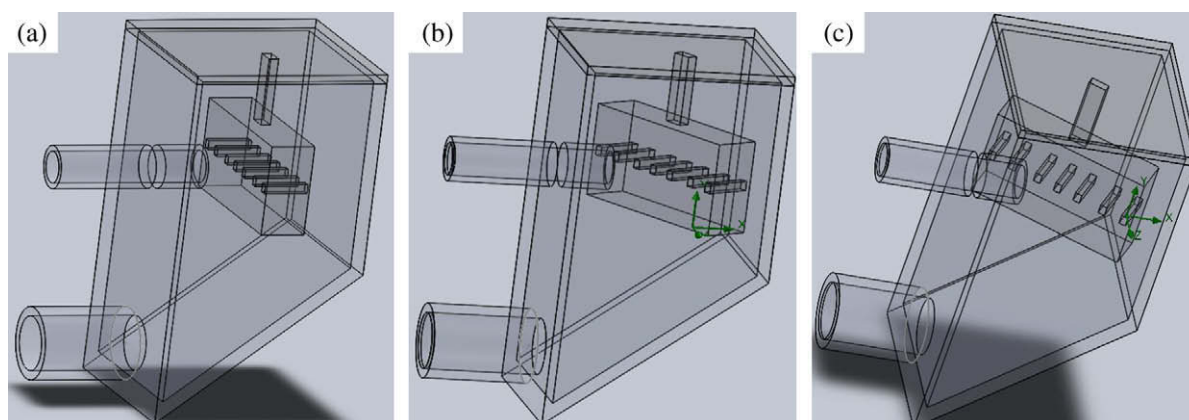| Ions	Na$^+$	K$^+$	Mg^{2+}	Ca^{2+}	Cl$^-$	SO$_4^{2-}$	HCO$_3^-$	Total ion concentration
Concentration (mg/L)	35,820	1152	749	6235	69,222	288	353	113,819

Fig. 2. Schematic diagram of the test chamber where the micro-electrodes are installed at various impact angles (a) 90°, (b) 60° and (c) 30°.

concentration in the solution favoured the formation of iron carbonate scale.

Potentiodynamic scan was carried out at a potential sweep rate of 1 mV/s after the steel electrode reached a relatively steady state, which was indicated by a stable corrosion potential. It was usually considered as a steady state if the fluctuation of corrosion potential was less than 2–3 mV. Moreover, linear polarization measurement was conducted at a scan rate of 10 mV/min to determine corrosion rate of the steel, with a ±15 mV relative to corrosion potential. Electrochemical impedance spectroscopy (EIS) was measured at corrosion potential with a sinusoidal potential excitation of 10 mV in the frequency range from 20 kHz to 10 mHz.

2.4. Surface characterization

After electrochemical test, micro-electrodes were removed and rinsed with deionized water. The surface morphology of the electrode was observed by SEM (Model Philips XL30).

3. CFD simulation

The CFD simulation was performed using a commercial software package of Solidworks 2009. Fig. 2 shows the diagram of test chamber and micro-electrodes for the FAC test at various impact angles. The fluid was assumed to be incompressible, and a $\kappa - \varepsilon$ turbulent model was used to numerically solve all simulation, where κ refers to the turbulent kinetic energy and ε refers to its local rate of dissipation. Turbulence intensity was set at 10%. The turbulent kinetic energy, κ, was set as 1 J/kg and the turbulent dissipation, ε, was 1 Wkg for simulation. The initial and boundary conditions for CFD simulation included:

(1) Inlet: a flow of aqueous solution with a velocity of 3 m/s.
(2) Outlet: an environment pressure of 101,325 Pa.
(3) The grid resolution: 0.4 mm.
(4) Solid wall: the wall could be approximately considered as an adiabatic wall with a roughness of 10 μm, and the surface of electrode was also set at 10 μm.
(5) Flow type: turbulent flow as calculated.

4. Results

4.1. Polarization curves measurements

The polarization curves measured on the individual micro-electrodes at different impact angles are shown in Fig. 3, where polarization curves measured on micro-electrodes 5, 6 and 7 at the impact angel of 90° were not shown because these electrodes were symmetrical to micro-electrodes 1, 2 and 3, respectively. It is seen that all curves showed an actively controlled anodic process and a mass transfer-controlled cathodic process. When the impact angle changed, there was little effect on the anodic current density, while the cathodic current density changed remarkably. At the normal impact, i.e., the normal angle was 90°, there was the smallest cathodic current density on electrode 4, which was located at the center of the holder. From micro-electrodes 1, which was on the edge of the holder, to micro-electrode 3 that was adjacent to the center, the cathodic current density increased. At an impact angle of 60°, there was a higher cathodic current density on electrodes that were away from the nozzle, e.g., micro-electrodes 1, 2 and 3, and a lower cathodic current density on those that were close to the nozzle, e.g., micro-electrodes 5, 6 and 7, with the highest and lowest cathodic current densities on micro-electrodes 3 and 7, respectively. When the impact angle decreased to 30°, the cathodic current density of the electrodes that were far away from the nozzle further increased, while those close to nozzle decreased.
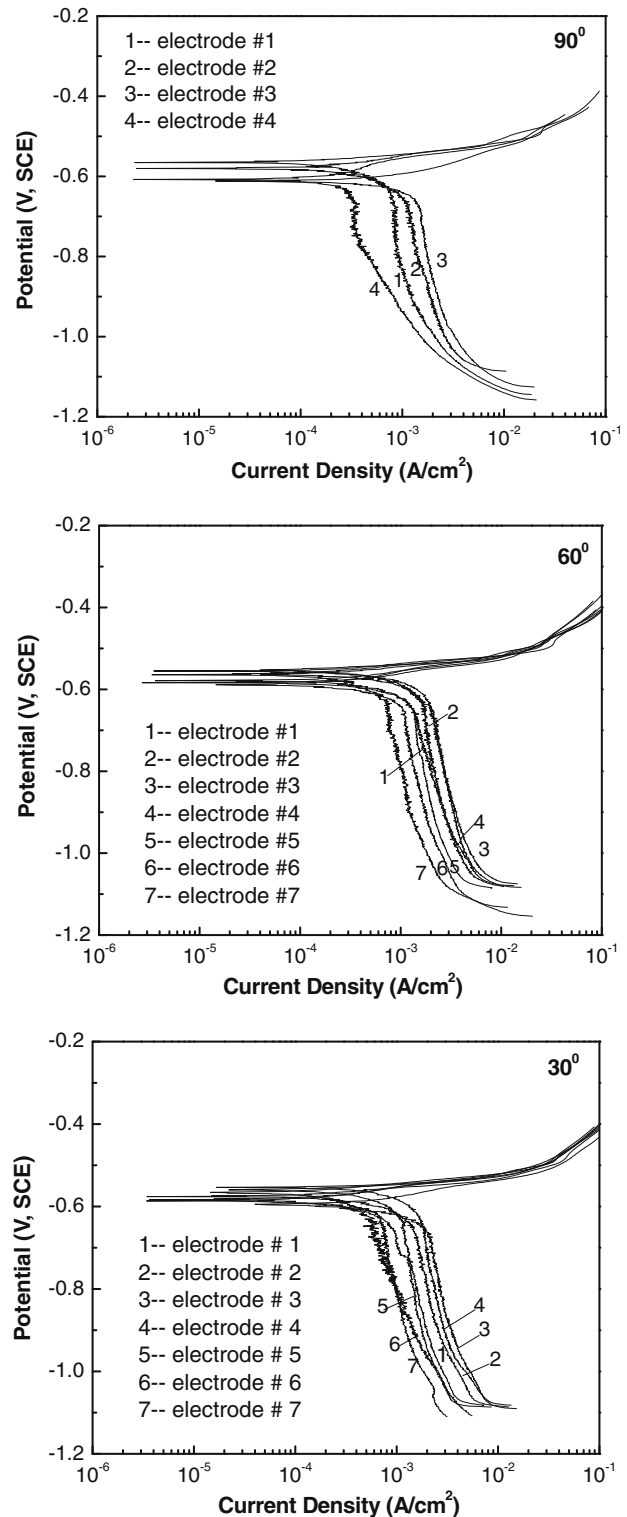

Fig. 3. Polarization curves measured on the individual micro-electrodes at various impact angles with a flow velocity of 3 m/s.

Fig. 4 shows the corrosion rates of the micro-electrodes at different impact angles determined by the linear polarization resistance measurements. The quite high corrosion rate on the order of magnitude of mA/cm^2 is due to the enhancing effect of fluid impact on the electrode. At an impact angle of 90°, the lowest and highest corrosion rates were observed on micro-electrode 4 and micro-electrodes 3 and 5, respectively, which were located at the
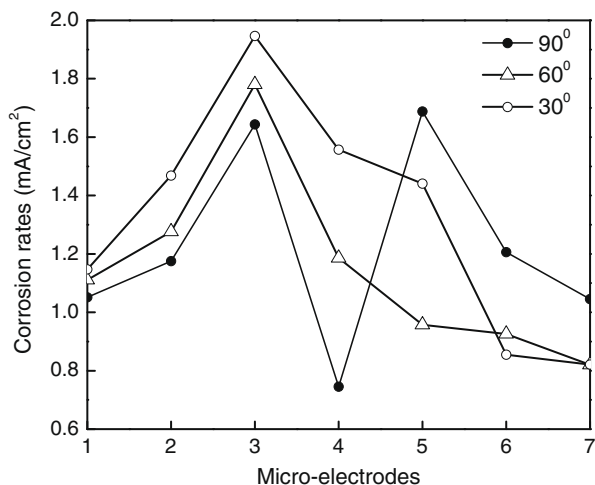
Fig. 4. Corrosion rates of the individual micro-electrodes at various impact angles with a flow velocity of 3 m/s.

center of the holder and adjacent to the center. With the electrodes far away from the center, the corrosion rate decreased. At the impact angle of 60°, the highest corrosion rate was observed on micro-electrode 3 that was next to the center at the side away from the nozzle. The corrosion rates of the micro-electrodes away from the nozzle were higher than those at the side close to nozzle. When the impact angle was 30°, the corrosion rates of the micro-electrodes followed the identical pattern to those determined at an angle of 60°. However, the highest corrosion rate increased with the decrease of the impact angle.

4.2. Electrochemical impedance spectroscopy measurements

The EIS plots measured on the individual micro-electrodes at different impact angles are shown in Fig. 5. Similarly, the EIS measured on micro-electrodes 5, 6 and 7 at the impact angel of 90° were not shown because they were symmetrical to micro-electrodes 1, 2 and 3, respectively. It is seen that there was an identical feature of all plots, i.e., one depressed capacitive semicircle in the high frequency range and one inductive semicircle in the low frequency range. While the high-frequency capacitive semicircle is attributed to the interfacial charge-transfer reaction, the inductive semicircle at low frequency is usually related to the adsorbed intermediate product formed during dissolution of the steel [24,25].

At the impact angle of 90°, there was a largest and smallest capacitive semicircle, which represents the charge-transfer resistance, on micro-electrodes 4 and 3, respectively. At an impact angle of 60°, the small semicircles were observed on micro-electrodes away from the nozzle, with the smallest semicircle on micro-electrode 3. For those close to the nozzle, there were generally large semicircles, with the largest one on electrode 7. When the impact angle decreased to 30°, the size of the semicircles far away from the nozzle further decreased, and those that were close the nozzle increased.

To analyze and derive the impedance parameters, an electrochemical equivalent circuit shown in Fig. 6 was used. The values of the fitted impedance parameters are listed in Table 2. It is seen that, for micro-electrode 4, the charge-transfer resistance decreased with the decreasing impact angle, indicating that a decrease of the fluid impact angle would increase the corrosion rate of the steel electrode.

4.3. CFD simulation

Fig. 7 shows the cross-sectional and surface views of the CFD simulation of fluid flow field exerted on the electrodes at various
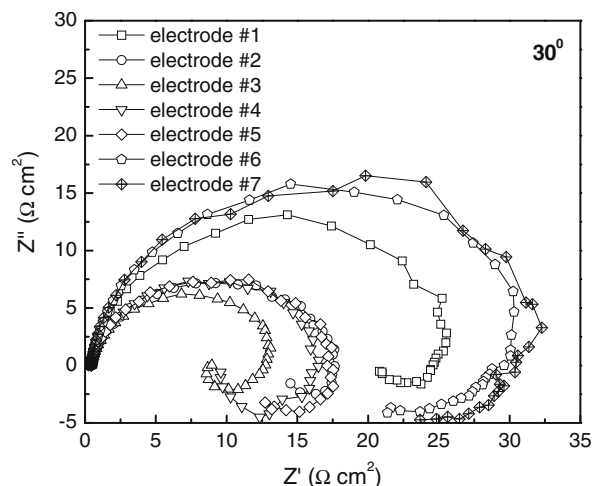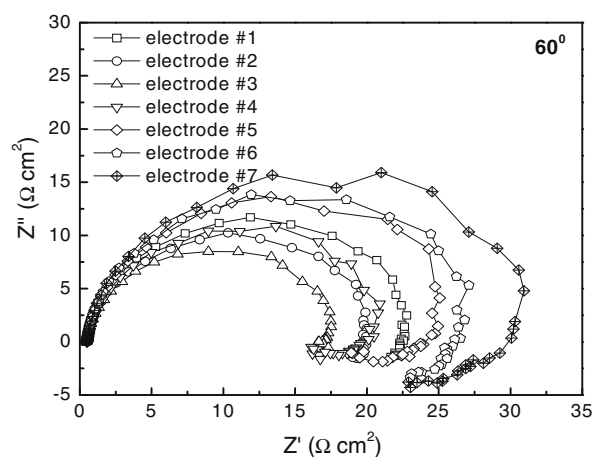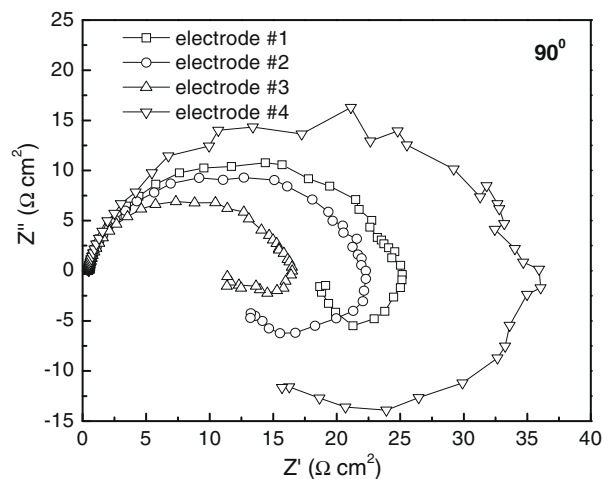

Fig. 5. EIS plots measured on the individual micro-electrodes at various impact angles with a flow velocity of 3 m/s.

impact angles with a fluid flow velocity of 3 m/s. It is seen that, at an impact angle of 90°, the flow field is center-symmetrical, with the lowest velocity of about 1 m/s in the centric region, and the highest velocity of 2.3 m/s at micro-electrode 3 and 5 that were located adjacent to the center. When the electrode was further away from the center, the flow velocity decreased.

When the impact angle was 60°, the flow field was not symmetric. A high flow velocity was observed on micro-electrodes 2, 3 and 4 that were away from the nozzle, with the highest flow velocity of
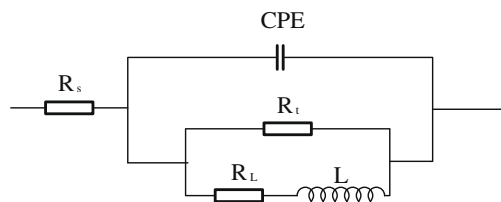
Fig. 6. Electrochemical equivalent circuit for fitting the experimental impedance data, where R_s is solution resistance, CPE is constant phase element, R_{ct} is charge-transfer resistance, R_L is inductance resistance, and L is inductance.

about 2.5 m/s on electrode 3. At the side close to nozzle, there was a low velocity, with the lowest velocity of 0.6 m/s on electrode 7 that was located at the outmost from the center.

With a further decrease of the impact angle to 30°, the flow field distribution was asymmetrical too. Similar to the impact angle of 60°, the high flow velocity was observed on electrodes 2, 3 and 4. The highest velocity of 2.8 m/s was observed on electrode 3 and the lowest velocity of 0.3 m/s on electrode 7.

Fig. 8 shows the distribution of shear stress on the electrode surfaces at various impact angles. At an impact angle of 90°, the shear stress was distributed symmetrically. A low shear stress region was observed at the center, and the largest shear stress on electrodes 3 and 5 that were adjacent to the center. When the impact angle decreased to 60°, the shear stresses on the electrodes that were away from the nozzle were higher than those at the side close to nozzle. The highest shear stress was observed on electrode 3. With far away from the center, the electrodes had a decreasing shear stress. When the impact angle was 30°, the largest shear stress was observed at the center.

4.4. SEM surface morphology characterization

Fig. 9 shows the SEM views of the surface morphologies of the micro-electrodes after FAC test at the impact angle of 90°. The morphologies of the electrodes after test at the impact angles of 30° and 60° were quite similar to that tested at 90°. Only the SEM views tested at 90° were present to simplify the presentation of the results. It is seen that corrosion product scale was observed on all the electrode surfaces. The corrosion scale formed on electrode 3 was not compact, while that on electrode 4, which was

located at the center, was much more compact. The compactness of the corrosion scales on electrodes 1 and 2 were in between.

5. Discussion

5.1. Corrosion electrochemistry in CO_2-saturated formation water

It is acknowledged [26] that, when CO_2 dissolves into water, carbonic acid will form, which is more corrosive to carbon steel than a completely dissociated acid at the same pH value. The cathodic reactions during corrosion of carbon steel in the CO_2-saturated formation water include:

$$2H^+ + 2e \rightarrow H_2 \tag{1}$$
$$2H_2CO_3 + 2e \rightarrow 2HCO_3^- + H_2 \tag{2}$$
$$2HCO_3^- + 2e \rightarrow 2CO_3^{2-} + H_2 \tag{3}$$
$$2H_2O + 2e \rightarrow 2OH^- + H_2 \tag{4}$$

The dominant cathodic reaction depends on the pH of the solution [5]. At a low pH value, the H^+ reduction is the dominant cathodic process because of the high concentration of H^+. When pH increases to 4–6, the direct reductions of HCO_3^- and H_2CO_3 become important due to the decreasing H^+ concentration in CO_2–H_2O system [24]. At a high overpotential, the dominant cathodic reaction changes to the direct reduction of water. The mass transfer-controlled cathodic reactions, as indicated in the polarization curves in Fig. 3, show the diffusion of the reactants to the electrode/solution interface. Under fluid flow, the flow field exerted on the electrode surface would affect the mass transfer process of cathodic reactants, and then the corrosion reaction of the steel.

The anodic reaction in CO_2 corrosion of the steel is primarily the dissolution of steel through steps:

$$Fe + H_2O \rightleftharpoons FeOH_{ads} + H^+ + e \tag{5}$$
$$FeOH_{ads} \rightarrow FeOH^+ + e \tag{6}$$
$$FeOH^+ + H^+ \rightleftharpoons Fe^{2+} + H_2O \tag{7}$$

It has been suggested [27] that the dissolution of Fe in the CO_2-saturated solution follows a consecutive mechanism with the adsorbed intermediate product $(FeOH)_{ads}$. The presence of an inductive semicircle at low frequency of EIS plots (Fig. 5) indicates the adsorbed intermediate product on the electrode surface. Since

Table 2
Electrochemical parameters fitted from the measured EIS data.

| Electrodes	R_s (Ω cm^2)	Y_0 ($\times 10^{-3}$ Ω^{-1} cm^{-2} s^{-n})	n	R_{ct} (Ω cm^2)	R_L (Ω cm^2)	L (H cm^{-2})
Impact angle = 90°, flow velocity = 3 m/s						
Electrode 1	0.44	2.5	0.90	24.73	56.17	514.6
Electrode 2	0.44	2.7	0.90	22.12	20.08	256.2
Electrode 3	0.45	3.2	0.92	15.82	36.99	262.1
Electrode 4	0.46	2.1	0.90	34.87	10.62	435.2
Impact angle = 60°, flow velocity = 3 m/s						
Electrode 1	0.43	4.3	0.94	23.40	42.56	274.4
Electrode 2	0.44	5.2	0.93	20.37	34.52	195.4
Electrode 3	0.44	3.1	0.94	17.21	25.45	186.4
Electrode 4	0.45	1.8	0.95	21.92	43.54	234.3
Electrode 5	0.46	1.8	0.94	27.15	54.43	254.4
Electrode 6	0.44	1.9	0.94	28.09	64.79	375.5
Electrode 7	0.45	2.1	0.95	31.69	82.36	237.6
Impact angle = 30°, flow velocity = 3 m/s						
Electrode 1	0.43	3.2	0.88	24.83	22.13	436.4
Electrode 2	0.45	7.5	0.88	17.71	57.00	283.1
Electrode 3	0.42	8.2	0.90	13.36	23.61	133.8
Electrode 4	0.44	7.8	0.90	16.70	19.08	158.7
Electrode 5	0.45	8.5	0.86	18.05	22.64	382.3
Electrode 6	0.47	1.6	0.95	30.42	66.94	447.8
Electrode 7	0.42	2.2	0.95	31.66	66.34	666.9
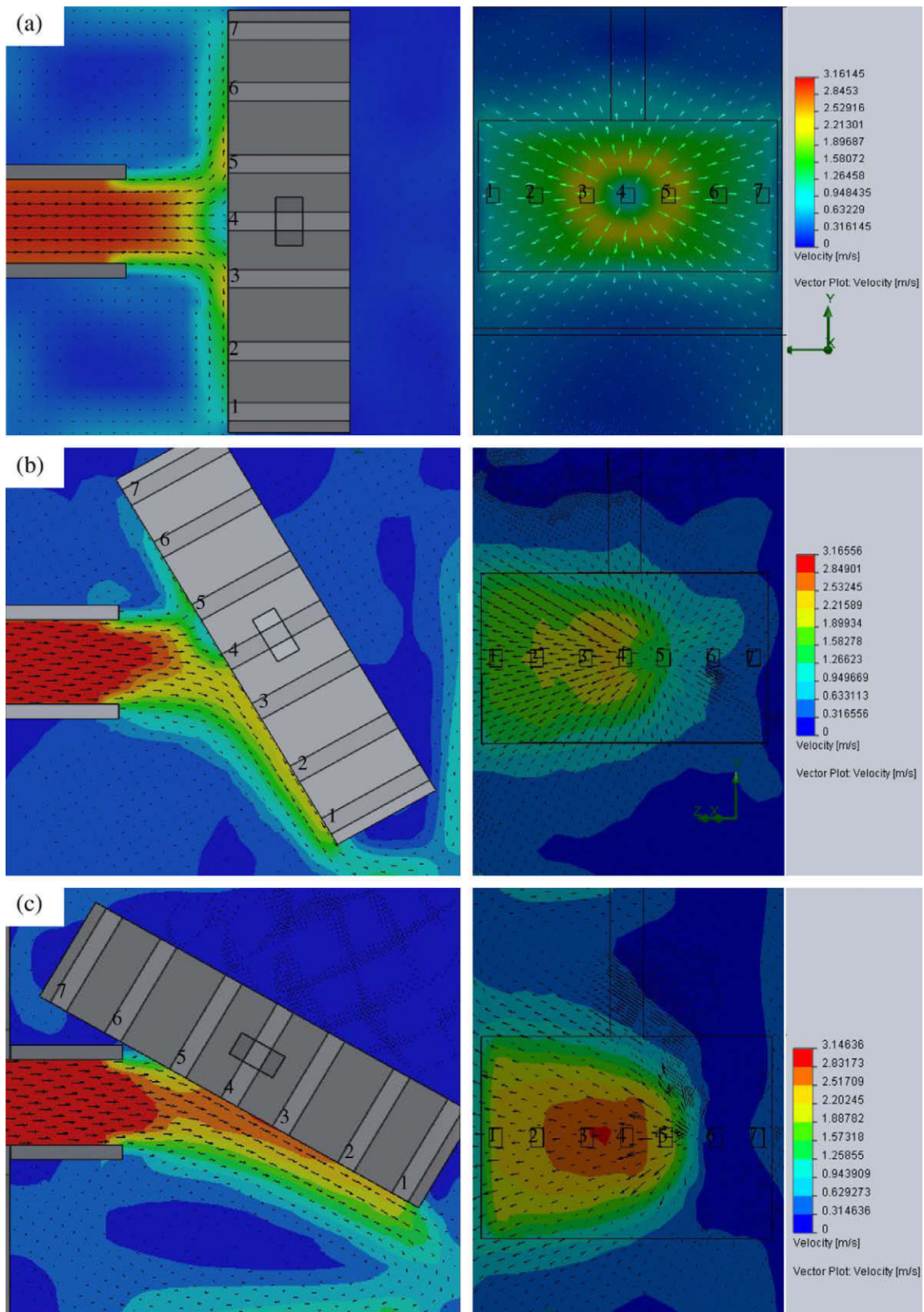
Fig. 7. Fluid flow field distribution on the micro-electrodes at different impact angles with a flow velocity of 3 m/s: (a) 90°, (b) 60° and (c) 30°.

the anodic process is controlled by an activation mechanism, rather than the mass transfer step, there is little influence of the flow field on the anodic reaction process, as shown in the measured polarization curves in Fig. 3.

During corrosion of the steel, the corrosion scale $FeCO_3$ would form on the steel surface either by a super-saturation to exceed the solubility product of the scale or by an electrochemical oxidation of Fe:
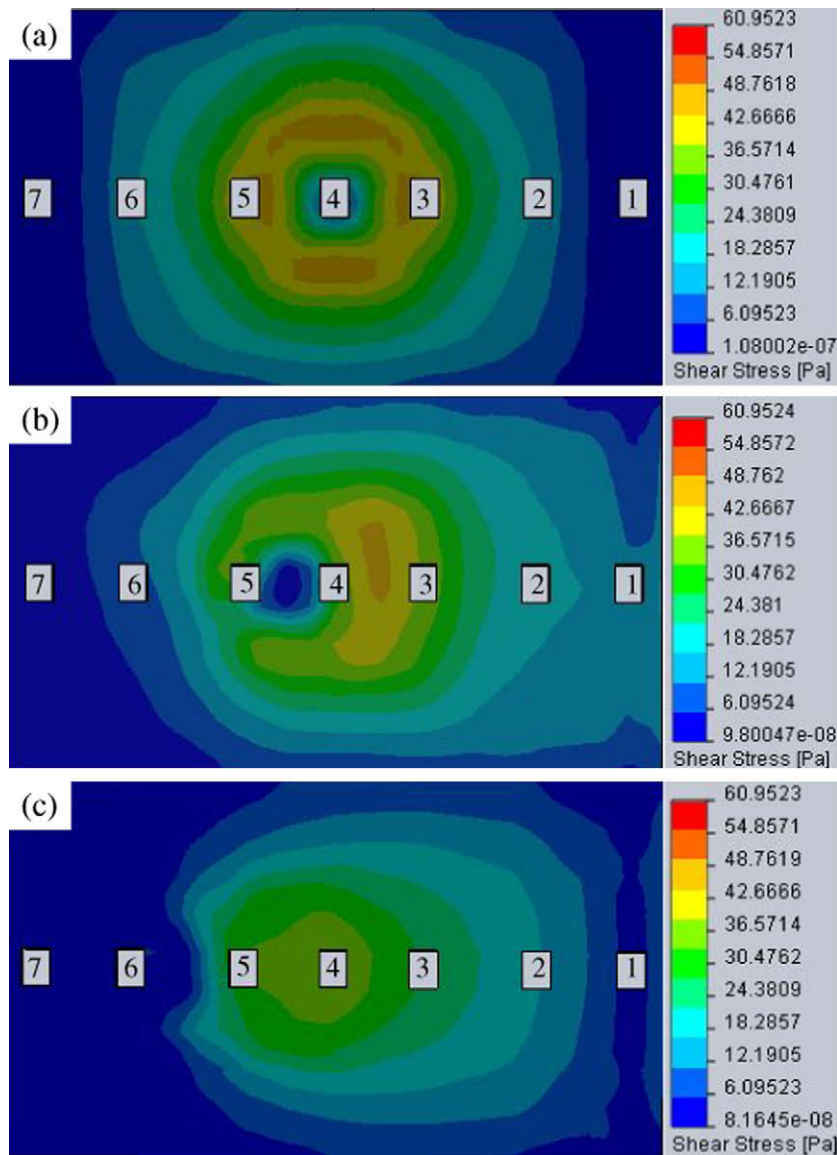
Fig. 8. Shear stress distribution on the micro-electrodes at different impact angles with a flow velocity of 3 m/s: (a) 90°, (b) 60° and (c) 30°.

$$Fe^{2+} + CO_3^{2-} \rightarrow FeCO_3 \tag{8}$$
$$Fe + HCO_3^- + e \rightarrow FeCO_3 + H \tag{9}$$

The $FeCO_3$ scale would provide somewhat protection to the steel substrate by a blocking effect. Other's work confirmed the formation of $FeCO_3$ scale on the steel surface at room temperature and atmospheric pressure [28]. They found that the product scale actually consists of both $FeCO_3$ and Fe_3C. Under fluid flow, the corrosion scale is degraded or even completely removed by the impact of fluid. It is thus expected that the flow field would affect the morphology, structure and the protectiveness of the scale. As seen in Fig. 9, the surface morphologies of the scales formed on various micro-electrodes show quite different compactness that under different flow fields.

5.2. Effect of fluid hydrodynamics on CO_2 corrosion of the steel

The CFD simulation indicates that there are quite different flow velocities and shear stresses at different regions along the radial direction under a normal impact of the fluid. The present simulat-

ing results are consistent with others' obtained previously [17,18]. The electrode under the impinging flow is generally divided into four regions: a central laminar region, a transition region, a wall jet region, and a boundary layer region [29]. In the centric region where the micro-electrode 4 is located, the flow is essentially laminar on the electrode surface, and the principal velocity component is changing from axial to radial, with a stagnation point at the center. The shear stress, which is the isothermal loss due to fluid friction resulting from contact with a stationary wall, is low at this region, as demonstrated in Figs. 7a and 8a.

With an increase of the radial distance to transition region, the fluid flow velocity increases rapidly and a maximum of velocity emerges at $\frac{x}{d} \approx 1$ (x is the radial distance from the center of the electrode and d is diameter of the nozzle). The shear stress increases to a maximum value, accompanying with the enhancement of the turbulence intensity over the electrode surface. The flow pattern is featured with a high turbulence, a large velocity gradient at the electrode surface, and a high shear stress. Thus, the transition region is of primary interest for studying fluid flow effects on corrosion in high turbulence areas. In this work, micro-electrodes 3 and 5 are located in this region.
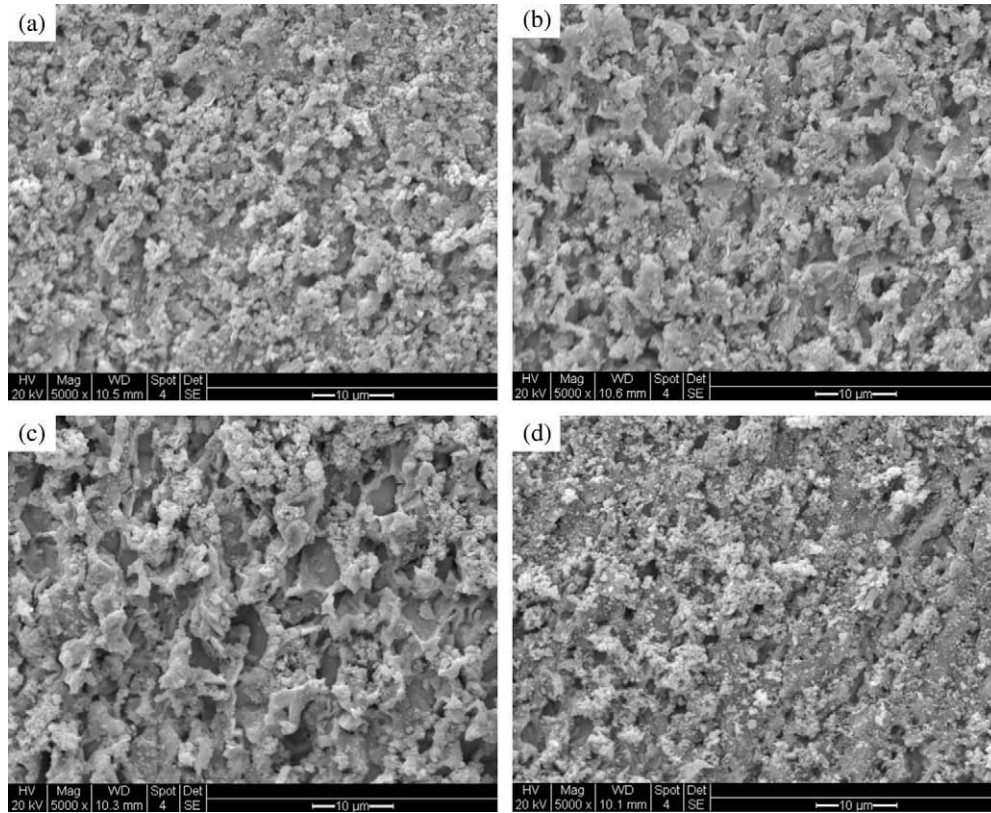
Fig. 9. SEM view of the surface morphologies of micro-electrodes after FAC test at an impact angle of 90° with a flow velocity of 3 m/s: (a) micro-electrode 1, (b) micro-electrode 2, (c) micro-electrode 3 and (d) micro-electrode 4.

The Sherwood numbers in the centric and transition regions are given by [30]:

$$Sh = 0.76Re^{0.5}Sc^{0.33} \quad \frac{x}{d} \leqslant 1.1 \tag{10}$$

$$Sh = 1.04Re^{0.5}Sc^{0.33} \quad \frac{x}{d} \leqslant 2.2 \tag{11}$$

where Sh is Sherwood number ($Sh = Kd/D$), Re is Reynolds number ($Re = Vd/v$), Sc is Schmidt number ($Sc = v/D$), V is the free jet flow velocity, D is diffusion coefficient, v is kinematic viscosity, and K is mass transfer coefficient. The mass transfer coefficients in the two regions are thus derived as:

$$K_{cen} = 0.76d^{-0.5}v^{-0.17}D^{0.67}V^{0.5} \quad \frac{x}{d} \leqslant 1.1 \tag{12}$$

$$K_{tran} = 1.04d^{-0.5}v^{-0.17}D^{0.67}V^{0.5} \quad \frac{x}{d} \leqslant 2.2 \tag{13}$$

It is obvious that the mass transfer rate in the transition region is higher than that in the centric region.

Electrochemical measurements, including polarization curve, linear polarization resistance and EIS measurement (Figs. 3–5), demonstrate that there are different electrochemical activities and corrosion behavior for micro-electrodes locating at different flow fields. Apparently, fluid hydrodynamics play an important role in FAC of the steel. As analyzed, in the CO_2-saturated formation water, the cathodic process is primarily mass transfer controlled. In the centric region, the low mass transfer rate results in a low cathodic current density and a low shear stress on the electrode surface. In the transition region, the high flow velocity, and thus the high mass transfer rate would enhance the transportation of reactive species towards the electrode surface, accelerating the cathodic reaction. Moreover, under the impingement of the fluid with a high shear stress, the $FeCO_3$ scale would be are removed continuously away by the fluid from the steel surface. The SEM

view (Fig. 9c) indicates a less compact corrosion scale present on the surface of micro-electrode 3.

With a further increase of radial distance ($\frac{x}{d} > 2$), the fluid flow velocity and turbulence intensity decay as the thickness of the wall jet increases and the surrounding fluid is entrained in the jet. The shear stress also decreases with the increase of the radial distance. The decreasing mass transfer rate and shear stress results in a decrease of corrosion rate of the steel, as seen in Fig. 4. At the boundary layer region, the flow velocity and the resulting shear stress further decrease, resulting in a further decrease of corrosion rate of the steel.

5.3. Effect of fluid impact angle on FAC of the steel

The electrochemical measurement and CFD simulation results show significant differences in corrosion of the micro-electrodes locating at different positions at oblique and normal impact angles. At the normal impact angle, the flow velocity and shear stress are centric-symmetric, with a maximum value at $\frac{x}{d} \approx 1$, resulting in a high corrosion rate. There is stagnation with a low flow velocity and shear stress in the centric region, which is associated with a low corrosion rate. At the oblique impact, the flow field distribution is asymmetric. There are high velocity and shear stress at the side far away from the nozzle, which cause the high corrosion rate of micro-electrodes at these positions. Furthermore, a decrease of impact angle would increase the differences of flow velocity, shear stress and corrosion rate between the side far away from the nozzle and that close to nozzle. For example, at the impact angle of 60°, the stagnation region shifts to the region between micro-electrodes 4 and 5 at the side close to nozzle, while at an impact angle of 30° this stagnation region further shifts to the edge of the sample holder, i.e., micro-electrode 7.

The flow velocity and shear stress in the centric region increases with the decrease of fluid impact angle, which results in an increasing corrosion rate in the centric region. The impact effect of fluid contains two components: the impact momentum in normal direction and the shearing motion in the lateral direction. The kinetic energy, E, of an impact fluid can be determined by Ref. [31]:

$$E = \frac{p^2}{2m} = \frac{mV^2}{2} \tag{14}$$

The components of kinetic energy at the normal direction and the lateral direction are determined as:

$$E_{normal} = \frac{(p \sin \phi)^2}{2m} = \frac{mV^2}{2} \sin^2 \phi \tag{15}$$

$$E_{lateral} = \frac{(p \cos \phi)^2}{2m} = \frac{mV^2}{2} \cos^2 \phi \tag{16}$$

where p is the impulse of fluid, m is the mass of fluid, and ϕ is the impact angle. The shearing effect in the lateral direction, $E_{lateral}$, would increases with the decreasing impact angle, enhancing the removal of corrosion scale. Therefore, the oblique impact generally results in a more serious degradation to the corrosion scale and causes a high corrosion rate of the steel electrode. At a normal impact angle, a normal stress is applied on the surface of electrode, and the corrosion scale would be damaged or ruptured, and not removed.

6. Conclusions

The role of fluid hydrodynamics in FAC of steel in the CO_2-containing solution depends on its effect on the carbonate corrosion scale formed on the electrode surface. An increasing flow velocity and shear stress would thinner, degrade or even remove completely the scale, increasing corrosion of the steel. During fluid impingement, the shearing effect in the lateral direction increases with the decreasing impact angle, enhancing the removal of the corrosion scale from the steel surface. Therefore, an oblique impact of fluid would generally result in a high corrosion rate of the steel.

The effect of impact angle on corrosion of the steel is attributed to the distribution of fluid flow field and shear stress on the electrode surface. At the normal impact, a low flow velocity and shear stress and thus a low mass transfer rate would be generated at the centric region. Consequently, a compact corrosion scale can be formed on the electrode surface to protect the steel from corrosion. The highest corrosion rate is observed on micro-electrodes that are adjacent to the center, with the highest flow velocity and shear stress. With a further increase of radial distance, the corrosion rate of the steel decreases because the flow velocity and shear stress decrease. At the oblique impact angles, the fluid flow velocity and shear stress, and the corrosion rate of the micro-electrodes are higher at the side far away from the nozzle than those at the side close to nozzle, which is resulted from the different distributions of fluid flow field and shear stress at both sides. The corrosion activity of the steel electrode located at the center of the sample holder generally increases with the decreasing impact angle due to the enhancing shear effect on the corrosion scale.

References

[1] D.A. Lopez, S.N. Simison, S.R. de Sanchez, Electrochim. Acta 48 (2003) 845.
[2] M.B. Kermani, A. Morshed, Corrosion 59 (2003) 659.
[3] B.R. Linter, G.T. Burstein, Corros. Sci. 42 (1999) 117.
[4] Z. Xia, K.C. Chou, Z.S. Smialowska, Corrosion 45 (1989) 636.
[5] S. Nesic, Corros. Sci. 49 (2007) 4308.
[6] K. Videm, J. Kvarekval, Corrosion 51 (1995) 260.
[7] T. Hong, Y.H. Sun, W.P. Jepson, Corros. Sci. 44 (2002) 101.
[8] G.I. Ogundele, W.E. White, Corrosion 42 (1986) 71.
[9] S. Nesic, J. Postlethwaite, S. Olsen, Corrosion 52 (1996) 280.
[10] D.A. Lopez, W.H. Schreiner, S.R. de Sanchez, S.N. Simison, Appl. Surf. Sci. 207 (2003) 69.
[11] G.T. Burstein, K. Sasaki, Corros. Sci. 42 (2000) 841.
[12] K.D. Efird, E.J. Wright, J.A. Boros, T.G. Hailey, Corrosion 49 (1993) 992.
[13] S. Zhou, M.M. Stack, R.C. Newman, Corros. Sci. 38 (1996) 1071.
[14] E.A.M. Hussain, M.J. Robinson, Corros. Sci. 49 (2007) 1737.
[15] K. Sasaki, G.T. Burstein, Corros. Sci. 49 (2007) 92.
[16] X. Hu, A. Neville, Wear 29 (2009) 2027.
[17] A. Gnanavelu, N. Kapur, A. Neville, J.F. Flores, Wear 267 (2009) 1935.
[18] A. Neville, C. Wang, Wear 267 (2009) 2018.
[19] H.Q. Becerraa, C. Retamosoa, D.D. Macdonald, Corros. Sci. 42 (2000) 561.
[20] L.Y. Xu, Y.F. Cheng, Corros. Sci. 51 (2009) 2330.
[21] G.A. Zhang, L.Y. Xu, Y.F. Cheng, Corros. Sci. 51 (2009) 283.
[22] X. Tang, L.Y. Xu, Y.F. Cheng, Corros. Sci. 50 (2008) 1469.
[23] L.Y. Xu, Y.F. Cheng, Corros. Sci. 50 (2008) 2094.
[24] G.A. Zhang, Y.F. Cheng, Corros. Sci. 51 (2009) 87.
[25] G.A. Zhang, Y.F. Cheng, Corros. Sci. 51 (2009) 1589.
[26] E. Gulbrandsen, Corrosion/2007, Paper No. 322, NACE, Houston, 2007.
[27] J.O.M. Bockris, D. Drazic, Electrochim. Acta 7 (1962) 293.
[28] E. Gulbrandsen, R. Nyborg, T. Loland, Corrosion/2000, Paper No. 23, NACE, Houston, 2000.
[29] Y.C. Lu, Corrosion/2004, Paper No. 677, NACE, Houston, 2004.
[30] J.L. Dawson, C.C. Shih, D.G. John, D.A. Eden, Corrosion/1987, Paper No. 453, NACE, Houston, 1987.
[31] K. Sugiyama, K. Harada, S. Hattori, Wear 265 (2008) 713.